

Chapter 1

Analysis

In this chapter the various parts of the analysis are explained. In Section ??, the simulations used to estimate the detector's ability to measure UPC processes are discussed. Section ?? explains the considerations that went into the triggers that were developed for this measurement. The selection of UPC events is detailed in Section ?. Extraction of the number of coherent J/ψ candidates is explained in Section ?. The determination of the detector's efficiency for measuring UPC events is explained in Section ?. Finally, Section ?? lays out the systematic uncertainties for the measurement.

1.1 ~~MC simulation~~ Physics generators and Monte Carlo simulations

Every physical measurement is the product of the underlying physics folded with the response of the detector used to do the measurement. In order to understand the underlying physical process, the detector's effect on the measurement must be understood and accounted for. As instruments become more and more complicated, the interplay among all of the many parts of the detector makes an analytic approach to the problem untenable. For this reason, the numerical technique of Monte Carlo (MC) simulation is often the most effective approach for describing detector effects.

MC simulations use random number generation to model the many statistical effects of particles interacting with different parts of the detector. First, particles are generated according to

theoretical distributions. These particles are then propagated through a simulation of the detector. As the particles pass through the detector, random numbers are ~~again~~ used to determine how these particles interact with the materials of the detector based on the known properties of the material. In this way, the theoretical distributions are convolved with a realistic model of the detector's response. A more detailed picture of how the detector shapes the underlying distributions emerges with each successive event. The final goal of the MC simulation is to produce a set of events that ~~are produced resemble as closely as possible the results that would be seen were the physical process to be measured by the detector~~ accurately reproduce what would be measured if the theoretical input describes nature well.

1.1.1 STARlight and particle gun MC in CMS

In this thesis, two ~~main classes of MC simulation~~ classes of generator input samples were used, STARlight and a particle gun. The STARlight samples corresponds to the theoretical calculations described in Section ??, while the particle gun produces particles with a user defined momentum distribution. For STARlight three different physical process are simulated; coherent J/ψ production, where the photon couples to the nucleus as a whole, incoherent J/ψ production, where the photon couples to a nucleon within the nucleus, and photon-photon interactions, where the photons from the two nuclei interact with each other to produce a pair of oppositely charge muons directly. All three STARlight samples contain a μ^+ and μ^- in the final state. The second class ~~uses PYTHIA6 to decay~~ simulates J/ψ s-produced particles with a user defined p_T and rapidity distribution ~~into muon pairs and isotropic decay to muon pairs in the J/ψ rest frame.~~

Because STARlight is not integrated into the standard CMS software framework (CMSSW), a simulation software chain with 5 steps was developed. First, STARlight is run in the specified mode, and a single file is created for each physics process. In step 2, the STARlight output file is converted to the Les Houches (LHE) format [?], and the momentum of the parent J/ψ or the initial photon-photon pair is added to the record of each event. The event record produced by STARlight only contains the final state particles. To process the events in parallel, the STARlight files are

subdivided in step 2, creating several LHE files from a single STARlight file. The LHE files are used as input to CMSSW.

Steps 3 to 5 take place within CMSSW. In step three the generated particles are propagated through the GEANT4 [?] detector simulation. This accounts for all the interactions with the detector and produces as output a format identical to the raw data that is recorded during data taking. Steps 4 and 5 are processed using the same software as in data taking. In step 4 the reconstruction software used during data taking is run on the output of the detector simulation. The output of the reconstruction is reduced to the information that is needed for the final analysis in the final step.

The particle gun samples were created entirely within CMSSW. J/ψ mesons were created according to user defined p_T and rapidity distributions. ~~PYTHIA6 [?] decays the~~ The decay of J/ψ s to μ^+ and μ^- was simulated with a a uniform decay distribution, corresponding to unpolarized J/ψ particles. As with the STARlight samples, these muons are propagated through the GEANT4 simulation of the detector, and the raw data is produced. The remaining steps of running the reconstruction code and reducing the data to the final data needed for the analysis are identical to the STARlight production.

The momentum of the final state muons is the main drivers of whether the candidate can be measured. One of the two daughters muons must have enough momentum to fire the trigger, and both muons must have enough momentum to be reconstructed and tagged as a muon. There are at least 10 interactions lengths of material through which the muons must travel in order reach the muon chambers (see Fig. ??). This imposes an ~~effect~~ effective momentum threshold on which muons can fire the trigger and be reconstructed.

The p_T distribution and the polarization of the J/ψ s produced are the main factors controlling the momentum of the muon daughters, which vary for the different MC samples. The polarization effects how the momentum is shared between the daughters [?]. In the rest frame of the parent J/ψ , equal momentum is given to each daughter muon. However in the lab frame of the detector, the muon daughters which are emitted from transversely polarized J/ψ will tend to be emitted in the direction the J/ψ is traveling and will have unequal momentum in the lab frame. The daughter

traveling in the direction of the J/ψ will have increased momentum, whereas the daughter traveling opposite to the J/ψ direction will have decreased momentum.

In Fig. ?? the p_T of J/ψ s from the ~~coherent~~, STARlight generated coherent, and incoherent, and ~~the dimuon~~ p_T for photon-photon samples are compared. Both the coherent and the photon-photon samples are concentrated at low p_T , and neither sample extends much beyond 0.15 GeV. The incoherent sample is peaked near 0.5 GeV and extends beyond 1 GeV. The two particle gun samples resemble the incoherent and coherent samples p_T distributions. The first sample has a Gaussian p_T distribution extending to approximately 0.15 GeV, whereas the second is flat in p_T up to 2 GeV.

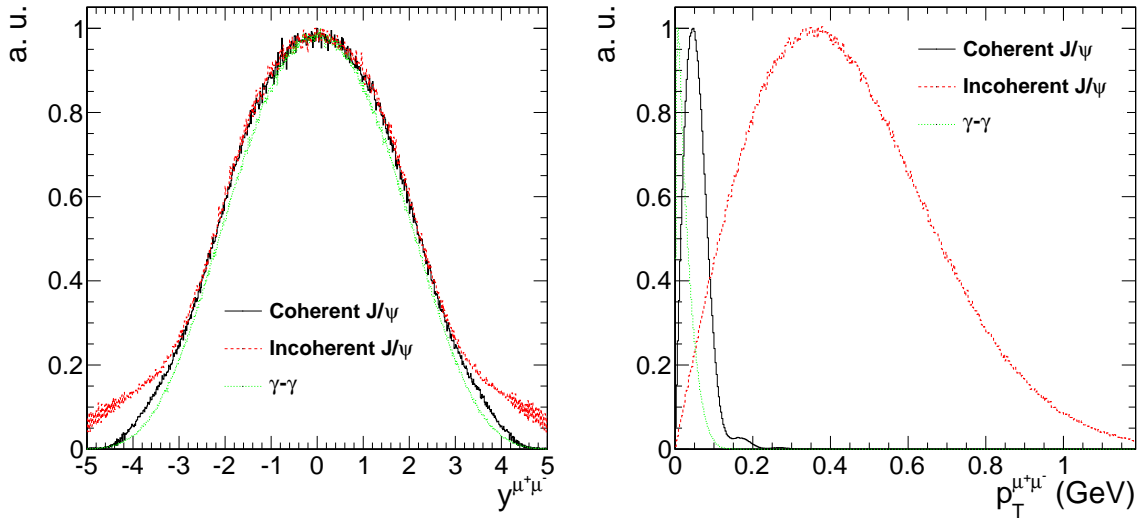


Figure 1.1: Generator level rapidity (left) and p_T (right) distributions for the coherent (black), incoherent (red), and photon-photon process (green).

The particle gun samples are unpolarized, whereas the STARlight samples have transverse polarization. In Fig. ??, the cosine of the helicity angle of the particle gun samples and the STARlight samples are shown. For the STARlight sample the helicity angle, the angle between the direction of the μ^+ daughter and the J/ψ direction in the rest frame of the J/ψ , prefer to be either parallel or antiparallel. However, the particle gun samples have no preferred direction of emission.

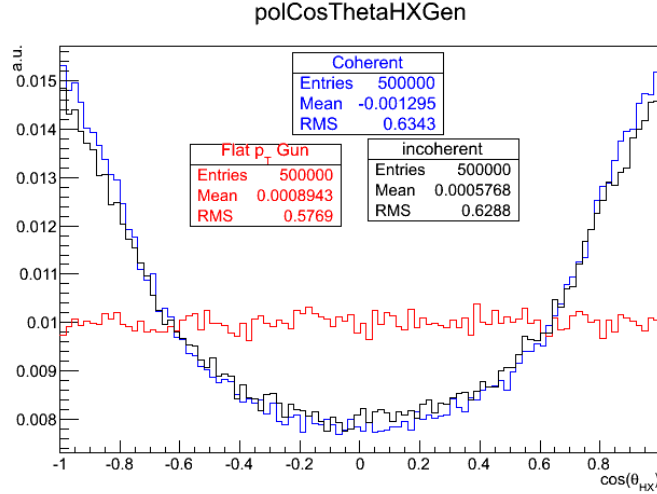


Figure 1.2: The J/ψ polarization of the particle gun (red), coherent (blue), and incoherent samples are plotted as the cosine of the helicity angle.

1.2 Trigger development

A collection of triggers was needed in order to select UPC events from the collisions at the LHC.

The increase in collision rate of the LHC PbPb beams from 2010 to 2011 was nearly a factor of 15. To accommodate this increase in rate, the 2011 trigger scheme needed to be more selective than in 2010 where CMS could take any event which appeared to have a collision. The available bandwidth was allocated equally amongst the various heavy ion analysis groups to pursue as wide a physics program as possible. From this consideration, bandwidth limits were placed on the trigger rates for each analysis group's trigger package. To ensure that UPC physics could be explored all while respecting the goals of the CMS Heavy Ions group as a whole, a ~~collection of~~ UPC triggers were commissioned.

The UPC trigger ~~for rate estimates for commissioning the 2011~~ ~~were created~~ triggers were calculated by combining existing triggers from the 2010 run. By calculating the ratio between the UPC trigger rates and the minimum bias trigger rate, the UPC trigger rates were scaled up to the anticipated 2011 interaction rates using the 2010 data. The trigger package for 2011 contained ZDC based efficiency monitoring triggers, muon and electron based triggers for measuring J/ψ , and backup triggers in case there was a problem with the original muon and electron triggers.

1.2.1 L1 trigger

The ~~goal of the~~ UPC L1 triggers were designed to record enough data to measure UPC J/ψ production via the dimuon and dielectron channels. To achieve this, the loosest muon and electron triggers were paired with a trigger on energy in the ZDC ~~and a veto on~~ were used as a trigger selection criteria, and energy in the BSCs was used as a rejection criteria. Additional triggers ~~that vetoed with rejection criteria based~~ on energy in HF were commissioned in case radiation damage during the run reduced the sensitivity of the BSCs. These triggers are summarized in Table ???. The 5 and 2 in the ECAL trigger names in Table ??? indicate a 5 and 2 GeV threshold on E_T measured in the ECAL. The Open in the muon trigger indicates that the trigger only requires a muon candidate in one of the three muon sub-systems and that there is not momentum threshold.

L1 trigger	Rate (Hz)	Prescale	Id	Type
MuonOpen and (ZDC ⁺ or ZDC ⁻) and BSC veto	2.1	1	1	Physics
ECAL2 and (ZDC ⁺ or ZDC ⁻) and BSC veto	1.8	2	2	
ECAL5 and (ZDC ⁺ or ZDC ⁻) and BSC veto	0.3	1	3	
(ZDC ⁺ or ZDC ⁻)	35	1500	4	Monitor
MuonOpen and (ZDC ⁺ or ZDC ⁻) and HF veto	0	off	5	Backup
ECAL2 and (ZDC ⁺ or ZDC ⁻) and HF veto	0	off	6	
ECAL5 and (ZDC ⁺ or ZDC ⁻) and HF veto	0	off	7	

Table 1.1: List of 2011 L1 seeds.

The cumulative L1 trigger rate for all the UPC L1 trigger seeds was required to be no greater than 200 Hz. This requirement stemmed from the need to keep the tracker read-out rate low. The trackers baseline voltage can fluctuate due to the high tracker hit multiplicities in PbPb collisions. In order to monitor the zero suppression of the tracker, the zero suppression algorithm was executed using the HLT computing farm rather than in the tracker firmware.

In order to record the efficiency monitoring data, the ZDC triggers had to be prescaled to a lower rate. The scaling down of the monitoring trigger was setup to ensure overlap with the signal triggers. The prescales for the triggers were set to balance the competing objectives of rate reduction and increasing the overlap between the monitoring and signal triggers.

1.2.2 HLT trigger

An event must pass the selection criteria of an HLT path in order to be recorded. As opposed to the L1 trigger, which has access only to information from calorimeters and muon chambers, the HLT has access to all ~~the~~ of the CMS sub-detectors including the tracker. Reconstruction of a track in the pixel detector is used by the UPC trigger paths. The use of the pixel detector only, as opposed to using the whole tracker including the silicon strip detector, allows for quick track reconstruction saving computing cycles. The requirement of at least one reconstructed pixel track for the HLT triggers was designed to reject backgrounds where no particles are reconstructed by the tracker. For the muon trigger in Table ?? the rate was reduced by nearly a factor of 4 compared to its L1 seed rate in Table ?. This is due to the additional pixel track requirement.

HLT trigger	Rate (Hz)	L1 prescale	HLT prescale	L1 seed	Type
L1UPCMuon and Pixel Track	0.52	1	1	1	Physics
L1UPCECAL2 and Pixel Track	1.65	2	1	2	
L1UPCECAL5 and Pixel Track	0.26	1	1	3	
L1ZDCOr	3.6	1500	11	4	Monitor
L1ZDCOr and Pixel Track	2.8	1500	1	4	
L1UPCMuonHFVeto and Pixel Track	0	off	off	5	Backup
L1UPCECAL2HFVeto and Pixel Track	0	off	off	6	
L1UPCECAL5HFVeto and Pixel Track	0	off	off	7	

Table 1.2: List of 2011 HLT trigger.

The total HLT output for the UPC trigger package was limited to 20 Hz. The limiting factor for the HLT rate was the amount of disk space available to store the data. To meet the bandwidth requirements and collect a significant sample of data for estimating efficiencies, the prescales were balanced with the goal of achieving at least 5% statistical precision on the efficiency estimates. As an example of the balancing of the prescales, the ZDC trigger that was passed through from the L1 was given a additional prescale factor of 11 on the HLT. The ZDC path that also required a pixel track on the HLT, which used the same L1 seed, was only prescaled at the L1. The prescale of 11 was set to ensure that at least 1000 of the pixel track ZDC triggers overlapped with the ZDC L1 only triggers so that efficiency of the pixel track requirement in the trigger could be estimated from

the tracks lost.

1.3 Event selection

~~In order~~ The unprecedented amounts of data produced by the LHC has made it possible to investigate novel physics processes like UPC J/ψ production, ~~the LHC has delivered unprecedented amounts of data~~. The data for this analysis ~~was~~ were recorded during the 2011 LHC PbPb run. During this period, $150 \mu b^{-1}$ ~~where~~ were recorded by the CMS detector, corresponding to over a billion PbPb collisions. Of this, $143 \mu b^{-1}$ of data were used in this analysis.

1.3.1 Data sets

~~Three~~ The data were dived into three specially selected samples ~~were used for this analysis~~, Physics, Monitoring, and Zero bias, based on the triggers which recored the events (see Table ??). By recording this hierarchy of samples, interesting events are selected with a much higher purity in the physics sample, while the zero bias and ZDC triggered samples allow for the investigation of the selection criteria. The purity, which is a measure of how many signal events relative to background events are in an sample, is obtained by using more selective triggers. Less selective triggers, those assigned to the monitoring and zero bias samples, were used to investigate to what extent signal events are lost due to the higher selectivity of physics triggers. These samples were recorded using subsets of the HLT triggers found in Table ?? of Section ?. The J/ψ events discussed in this thesis were obtained analyzing the sample labeled in Table ?? as physics. A ZDC triggered monitoring sample was recorded for the sake of estimating efficiencies. Lastly, a zero bias sample was recored for investigating the ZDC and the noise distributions of HF.

The physics sample containing the J/ψ signal was recorded by the muon trigger labeled "L1UPCMuon and Pixel Track" in Table ?. Because of the characteristically low momentum of UPC J/ψ as compared to J/ψ created by other physics processes, the loosest muon trigger was used. The noise trigger rate for the muon trigger alone was 50Hz, but in coincidence with the BCS veto and the

ZDC trigger the noise rate was below 2Hz. By pairing the muon trigger with the ZDC on the L1, the noise contribution was reduced from the noise contribution from either of the two sub-detectors to the noise coincidence between the two sub-detectors. Contributions from hadronic interactions are reduced by the veto on the BSCs. This trigger was designed to balance reducing the rate with maximizing the efficiency, allowing for the data to be recorded without producing high rates resulting in dead time for the detector.

In order to investigate the muon trigger and the other parts of the event selection, a monitoring sample was recorded by requiring energy consistent with at least one neutron in either of the ZDCs. ~~This process~~ Neutron production is much more common process than the UPC J/ψ production. ~~Neutron production~~ This process has cross sections on the order of 100 b compared to 10 mb predicted ~~from~~ for J/ψ production. For this reason, the rates of this trigger are much higher than the physics trigger, and only a small sub set of these events are recorded. From this trigger the pixel track portion of the HLT trigger efficiency was estimated as well as the ZDC trigger efficiency, as will be described in Section ??.

In addition to the monitoring and physics sample, a zero bias sample was recorded to examine the ZDC neutron reconstruction and the HF noise distributions. The zero bias trigger fired every time both beams passed through CMS. Only 4 events out of every million triggered were recorded for this sample. This sample allowed for an unbiased measurement of the ZDC neutron threshold energies as discussed in Section ?. Because the zero bias trigger does not require any activity in any of the CMS sub detectors, the sample contains very few hadronic collisions. This allowed for a measurement of the electronic noise distribution in the HF, which are important to reducing contamination from hadronic interactions.

The integrated luminosity for each of the three samples is calculated by recording activity in HF, the forward hadronic calorimeter in CMS [?]. The cross section for HF activity is measured from a van der Meer scan, and the cross section was found to be 45 mb for proton-proton running. In this way, the amount of integrated luminosity for any running period is related to the activity in HF.

Sample	Events	\mathcal{L}_{int}
Physics	346K	$143.3 \mu b^{-1}$
Monitor	1.1M	$31.6 mb^{-1}$
Zero Bias	8.8M	$580 b^{-1}$

Table 1.3: Integrated luminosities and number of events for the three samples used in this analysis.

Cut type	Cut	Events
–	all triggered	346841
beam background rejection	good vertex requirement	340997
	beam halo muon rejection	302777
	cluster shape compatibility requirement	233590
hadronic interaction rejection	single-sided neutron requirement	149992
	two track requirement	32732
	HF signal rejection	5392
fake muon rejection	muon quality requirement	2047
kinematic cut	J/ψ mass requirement	696
	muon detectability cuts	567

Table 1.4: Effects of event selection cuts.

1.3.2 Event selection cuts

The analysis described in this thesis focuses on UPC J/ψ s decaying to muons. The trigger used for this analysis recored 346841 events. A set of off-line cuts were applied to increase the relative contribution of UPC events to background processes. Two sets of event selection cuts were applied to reject background events. The first set rejects background from the beam. The second rejects events where hadronic collisions have occurred. Table ?? summarizes all the event selection cuts.

To reject beam induced background the following cuts were applied:

- The reconstructed vertex must be within 2 cm in the transverse direction and 25 cm in the longitudinal direction. This cut ensures that reconstructed particles come from interactions between the two beams rather than event where one of the two beams interact with gas particles near the interaction point.
- Beam halo muons were rejected using the timing of the muon hits. The beam halo cut rejects events where muons surrounding the beam stream through the detector.

- Pixel cluster shape should be compatible with the vertex. This cut requires that energy deposits in the silicon tracker point back to the reconstructed primary vertex.

These beam background cuts do not reject any UPC J/ψ candidates.

The second set of background rejection cuts were designed to reduce contamination from hadronic interactions.

- No more than 2 reconstructed tracks in the event. The track requirement rejects events that produce many charged particles.
- Maximum reconstructed hit energy in HF was required to be below the threshold for electronic noise. Nearly all hadronic interactions (about 98%) produce particles in the range $3 < |\eta| < 5$ covered by the HF detector. By requiring that the energy deposits in HF resemble noise, nearly all elastic hadronic collisions are expected to be rejected.
- Energy in the ZDCs consistent with neutrons on only one side of the interaction point. In hadronic interactions both nuclei break-up. By requiring that ZDC only reconstruct neutrons on one side of the interaction point, hadronic interactions that produce neutrons on both sides were rejected.

Each of these cuts were designed to reject topologies produced by hadronic interactions. The effect of these cuts can be seen in Table ?? and are denoted hadronic interaction rejection.

To establish the HF noise thresholds, the noise distributions were measured in zero bias events. An offline selection of events with no reconstructed tracks was used to ensure that no collision had taken place. The HF noise threshold was defined as the cut that keeps 99% of the zero bias events. The noise distribution from this zero bias sample is compared to the physics sample and MC in Fig. ??.

The following standard muon quality cuts are applied:

- Tracker track matched with at least one muon segment (in any station) in both X and Y coordinates ($< 3 \sigma$).

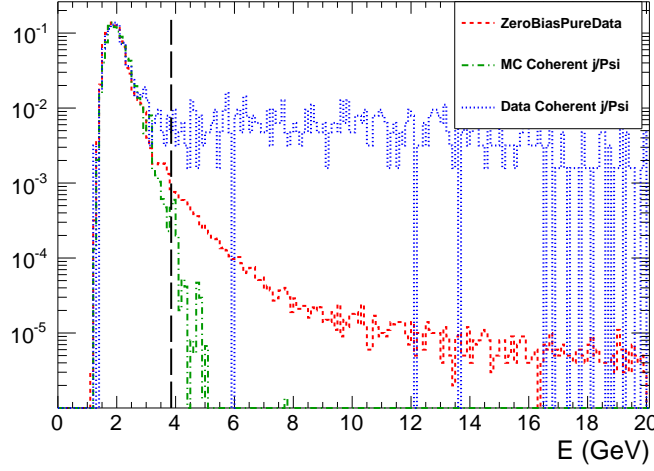


Figure 1.3: Comparison of HF noise distributions in zero bias data, physics triggered data, and MC.

- Cut on number of tracker layers with hits > 5 .
- Number of pixel layers > 0 .
- The χ^2 per degrees of freedom of the track fit < 3 .
- Loose transverse and longitudinal impact parameter cuts, with in 3 cm in the transverse direction and withing 30 cm in the longitudinal direction with respect to the primary vertex.

These cuts are applied to reduce the number of fake muons and have been validated for standard muon analyses.

1.4 Break up determination

As described in Section ??, UPC J/ψ photoproduction can be accompanied by the emission of neutrons from either of the two colliding nuclei. The various neutron emission scenarios, or break-up modes, can be distinguished by the two ZDCs. By separating events where the ZDC signal is consistent with 1 neutron versus several neutrons, or where neutrons are present on only one or both sides, the ~~different fraction of events which correspond to a given break-up modes can be separated mode can be measured~~ and compared to theory.

In order to maximize the ability to explore the one neutron peak, which sits at the bottom of the ZDCs dynamic range, a new ZDC reconstruction method was devised. This new reconstruction method was then used to establish a one neutron and many neutron threshold. This section describes the ZDC signal reconstruction and how the neutron thresholds on this signal were set.

1.4.1 ZDC signal reconstruction

The signal from each ZDC is built up from the pulse shapes for each of the 18 individual ZDC channels. The pulse shape is recorded in 250 ns second chunks and is divided into 10 time slices of 25 ns (See Fig ??). Counting from 0, the 4th time slice is synced with the timing of the rest of the detector and corresponds to when the products of the recorded collision reached the ZDC. The channel signal is therefore taken from the 4th time slice.

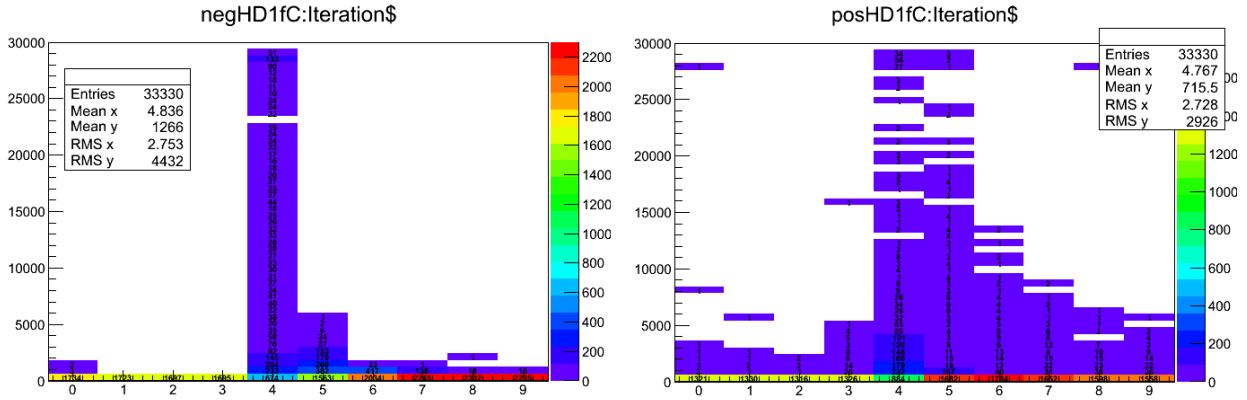


Figure 1.4: Average ZDC pluse shape is plotted as the charge as a function of time slice for the first hadronic from ZDC^- (left) and ZDC^+ (right).

The ZDC signal sits on top of a low frequency noise pedestal with a period of about 2μ seconds. Over the time scale of 250 ns, this low frequency noise signal appears as a constant that shifts randomly from event to event. The contribution from this noise is therefore measured event by event in order to subtract it. Time slice 5 is used for this purpose. Time slices 1 and 2 could also be used to estimate the low frequency noise. However because the noise fluctuates to negative values of charge that cannot be measured, these time slices can only provide a measurement of the noise half the time. By using time slice 5 which contains the falling tail of the signal, the noise can be

measured any time the signal raises significantly above the noise. If the fraction of signal in time slice 4 and 5 are constant and the noise contributes the same value to both time slices, the following formula is applicable:

$$Ts4 \propto (Ts4 + C) - (Ts5 + C) = Ts4 - R_{Ts5/Ts4} Ts4 = Ts4(1 - R_{Ts5/Ts4}), \quad (1.1)$$

where $Ts4$ is the signal contribution in time slice 4, $Ts5$ is the signal contribution to time slice 5, C is a random noise constant from the low frequency noise, and $R_{Ts5/Ts4}$ is the ratio between the signal contribution from time slice 5 over time slice 4. [Fig. Figure ??](#) demonstrates the consistence of the fraction and validates the unconventional method of using the falling tail of the signal to estimate the low frequency noise. By using time slice 5, the chances of measuring the noise are maximized. Separating the signal from the noise is especially important because the ZDC signal for the one neutron peak sits near the noise at the bottom of the ZDC dynamic range.

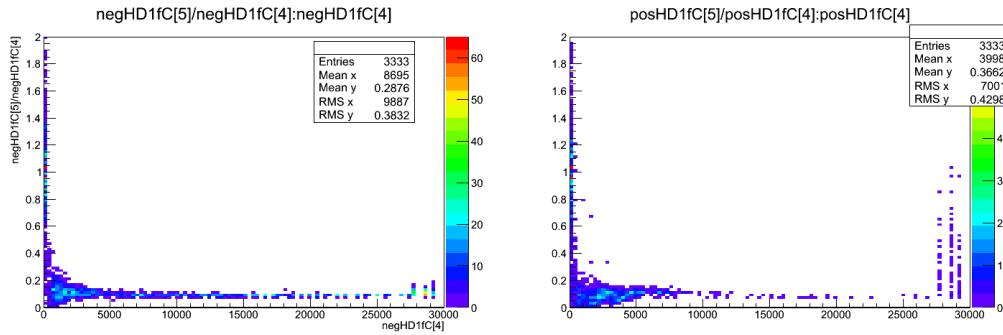


Figure 1.5: The fraction of signal in time slice 5 over time slice 4 as a function of the signal in time slice 5 in ZDC^- (left) and ZDC^+ (right).

When summing the 9 channels in each ZDC only channels with signals above zero in time slices 4 and 5 were included. The EM, [electromagnetic](#), section of the calorimeter is more densely packed with quartz fibers and therefore has a higher gain relative to the HAD, [hadronic](#), section. To account for this, the EM channels were weighted with a factor of 0.1 to match the HAD channel gains.

1.4.2 Determination of the one neutron thresholds

The ZDC thresholds used to establish the various break-up modes were measured from zero bias data. Figure ?? shows the weighted sum of the EM and HAD sections for ZDC^- and ZDC^+ for the zero bias dataset. The neutron spectrum for this dataset does is biased since the trigger only required that both beams were present in CMS. This does, however, include a significant electronic noise contribution due to events where no neutrons are emitted in the direction of the ZDC. It is clear from Fig. ?? that the gain of ZDC^+ is lower than that of ZDC^- . This is because of a damaged phototube on the first HAD section of ZDC^+ .

To determine the thresholds for one and multiple neutrons, the ZDC^+ and ZDC^- spectra were fit. Four Gaussian functions were combined to fit the spectra. The electronic noise was fit to a Gaussian around zero. The one, two, and three neutron peaks are fit to Gaussians that are successively broader. The mean of each peak was initially set to multiples of the mean of the one neutron peak. The threshold for a neutron in the ZDC was taken from the fits in Fig. ?. Any signal greater

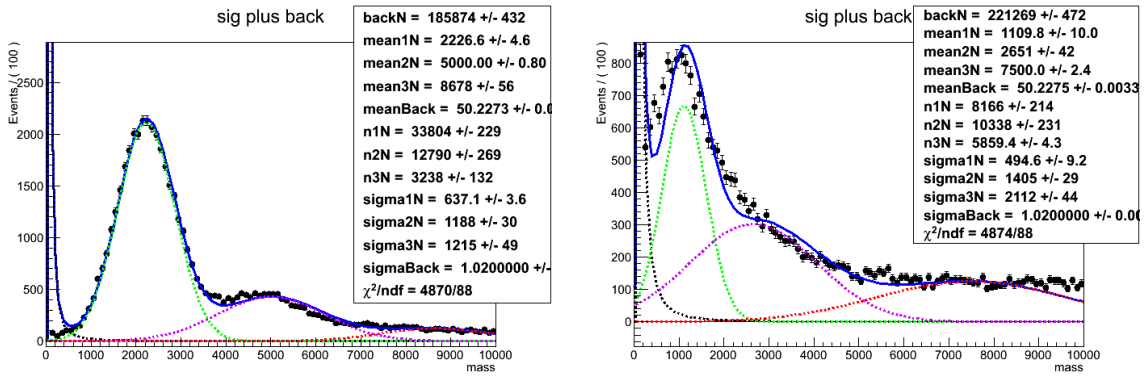


Figure 1.6: Fit to the signal spectra for ZDC^- (left) and ZDC^+ (right)

2σ below the mean of the one neutron peak was considered signal. Any signal greater than 2σ above was considered multiple neutrons. The single neutron break up modes were separated from the multiple neutron modes by use of these definitions.

Several of the break-up mode calculations that have been done involve single sided configurations where neutrons are present on one side of the interaction point and not the other. These modes can be hard to identify because the single neutron peak in ZDC^+ overlaps with the noise

peak at zero. To identify events where the ZDCs only measured noise, the noise spectrum were measured directly. Placing an additional criteria based on the ZDCs noise distributions for when the ZDCs are devoid of signal provides assurance that the events tagged as single sided events are truly single sided.

The noise distributions for the EM sections and the HAD sections were measured separately from out of time time slices. In Fig. ?? higher than average signal can be seen in the 0th time slice, which precedes the main signal time slice time slice 4 by 200 ns. This is due to events where activity was present in the ZDC for two consecutive collisions. Time slices 1 and 2, however, occurred between collisions. These time slices, which occur out of time, were used to measure the noise spectrum.

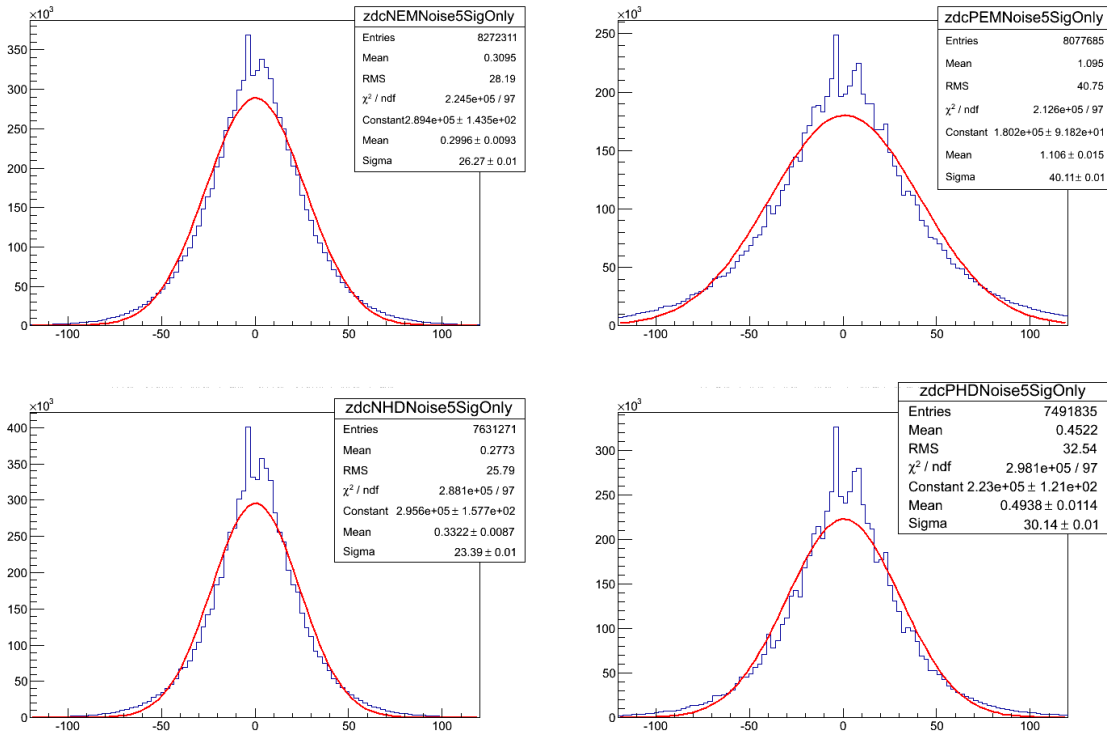


Figure 1.7: ZDC noise spectra from ZDC⁻ EM section (upper left), ZDC⁺ EM section (upper right), ZDC⁻ HAD section (lower left), and ZDC⁺ HAD section (lower right) from out of time time slices.

As with the signal measurements, the low frequency noise pedestal is subtracted event by event by subtracting time slice 2 from time slice 1 leaving only the high frequency noise. The noise

distributions do not depend on the amount of quartz fibers, but because the signal does, the noise distributions for EM and HAD sections are measured separately. Fig ?? shows the noise spectrum for each of the EM and HAD sections for the two ZDCs. If the HAD or EM signals measured from ~~the in time time-slices~~ time slices which match the timing for a collision, time slices 4 and 5, are less than 2σ above the mean of the noise distribution or lower, these sections are considered consistent with noise. A ZDC is considered consistent with noise if both the HAD section and EM section from that ZDC have signal measurements consistent with noise.

1.5 Signal extraction

After all event selection cuts, the remaining events contain a combination of coherent J/ψ , incoherent J/ψ , and dimuons from the photon-photon process~~all contribute to the remaining events~~. Each process must be separated from the final mix. To achieve this, the invariant mass and p_T distributions are used to distinguish between the three processes. The photon-photon process is extended in invariant mass whereas the J/ψ is peak strongly near 3.1 GeV. In dimuon transverse momentum distribution of the photon-photon and coherent process have similar distributions, both peaked sharply below 0.1 GeV, whereas the incoherent process is more broadly distributed across an interval extending to nearly 1 GeV. The mass distribution was fit to separate the photon-photon process from the J/ψ process. The p_T distribution was used to separate the incoherent process from the photon-photon process, and the coherent process. In this way, a separate yield was extracted for all three processes.

The invariant mass distribution for opposite sign dimuons is shown in Fig. ?. A J/ψ signal is clearly visible together with tails at higher and lower mass due to the photon-photon process. A fit to the invariant mass distribution was done using a Gaussian to account for the J/ψ signal and a first order polynomial function for the photon-photon process. The extracted number of J/ψ candidates from this fit includes all J/ψ s in the mass window that passed the analysis cuts, i.e. both coherent and incoherent process contribute to yield from the mass fit. The p_T distribution is

331 needed to separate the two different contributions to the J/ψ peak.

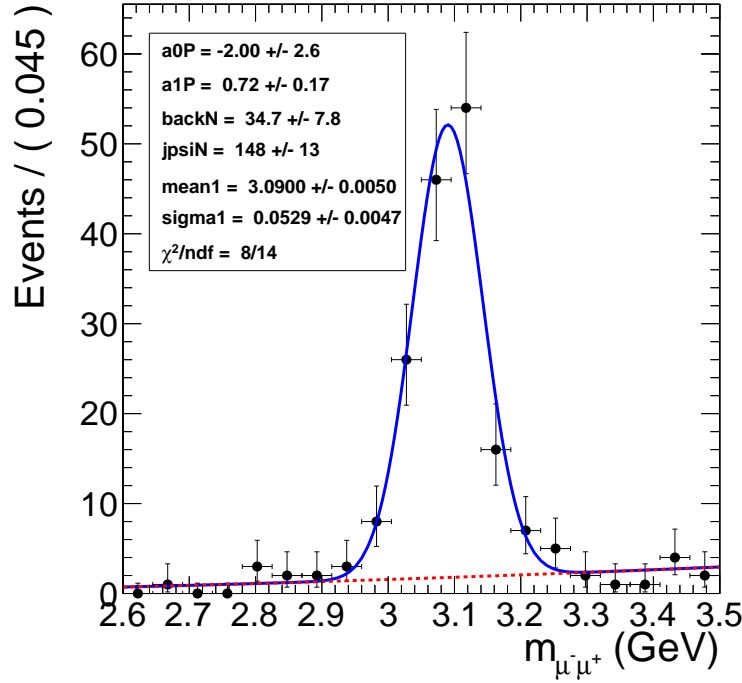


Figure 1.8: Mass fit to J/ψ using Gaussian for the signal and a first order polynomial for the photon-photon continuum

332 Figure ?? shows the p_T spectrum of the events plotted in Fig. ?. There is a clear coherent
 333 peak at $p_T = 60$ MeV followed by broad distribution that peaks near $p_T = 450$ MeV. To extract
 334 the contribution of coherent, incoherent and gamma-gamma processes in the data the spectrum
 335 in Fig. ? was fit to the sum of three MC templates corresponding to the final output of the MC
 336 simulations for these three processes. The clear overlap of the coherent and photon-photon process,
 337 and the clear separation of these two lower p_T processes from the incoherent process is apparent.
 338 The shape of the p_T distribution for the coherent, incoherent, and photon-photon process are taken
 339 from the final output of MC after applying all analysis cuts. In Fig.?, the yield parameters that
 340 were fit were left unconstrained for all three process.

341 The shape of the photon-photon and coherent J/ψ process are very similar in [transverse momentum](#).
 342 Accordingly, the contribution from the photon-photon process and the coherent process are diffi-
 343 cult to separate from the p_T distribution. The confidence contours in Fig. ? from the template

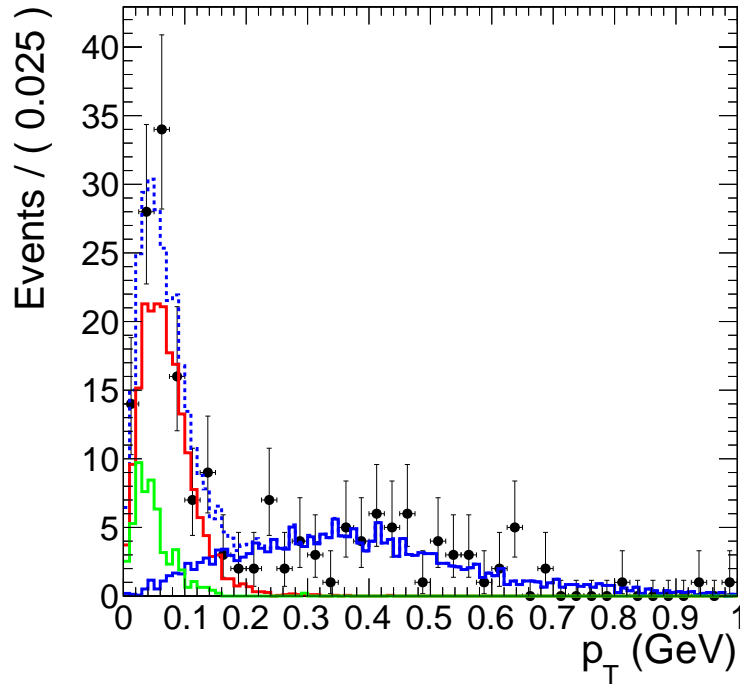


Figure 1.9: Fit to MC p_T templates.

fit in Fig. ?? demonstrate the strong anti-correlation between the coherent yield parameter, nCo , and the yield parameter for the photon-photon process, $nGamma$. Because of the anti-correlation, the statistical uncertainty on nCo and $nGamma$ from the fit are larger than \sqrt{nCo} and \sqrt{nGamma} expected from Poisson statistics. The information from the invariant mass and p_T distributions were combined to break this correlation. Through this combination, the contribution to the final yield from the three process was measured.

A simultaneous fit to the mass spectrum and p_T spectrum was preformed to utilize the mass fits ability to distinguish the photon-photon process from the coherent and incoherent process all while utilizing the p_T fits ability to separate the coherent and photon-photon processes from the incoherent. Fig. ?? shows the result of the simultaneous fit. The simultaneous fit forces the parameter $nGamma$ to both describe the photon-photon continuum present in the side bands of the J/ψ mass peak as well the photon-photon contribution to the low- p_T part of the p_T spectrum. In addition, the J/ψ yield from the mass fit is forced to equal the contribution from the incoherent and coherent process in the fit to the p_T distribution. In this way, the correlation between the yield parameters

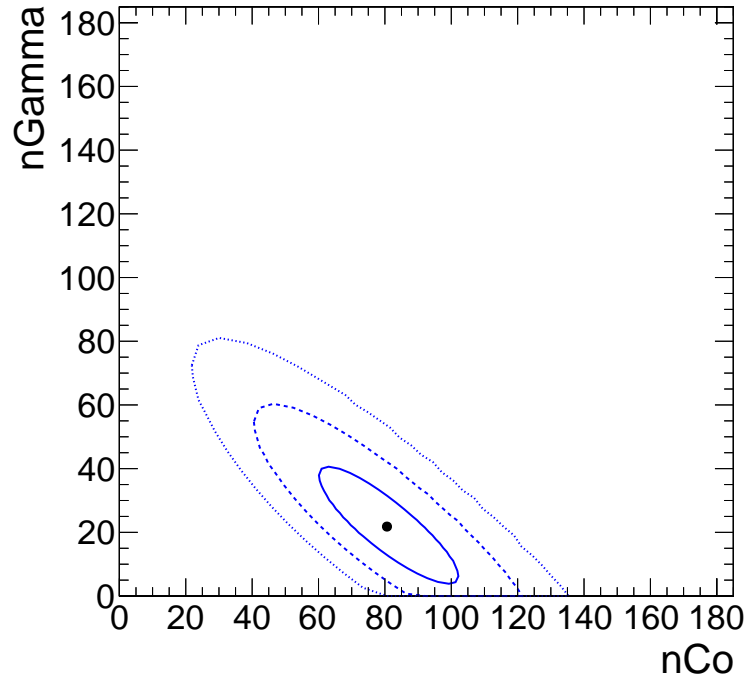


Figure 1.10: 68%, 95%, and 99% confidence contours from the p_T template fit.

358 was broken, and the contribution from the three process were made independent of each other.

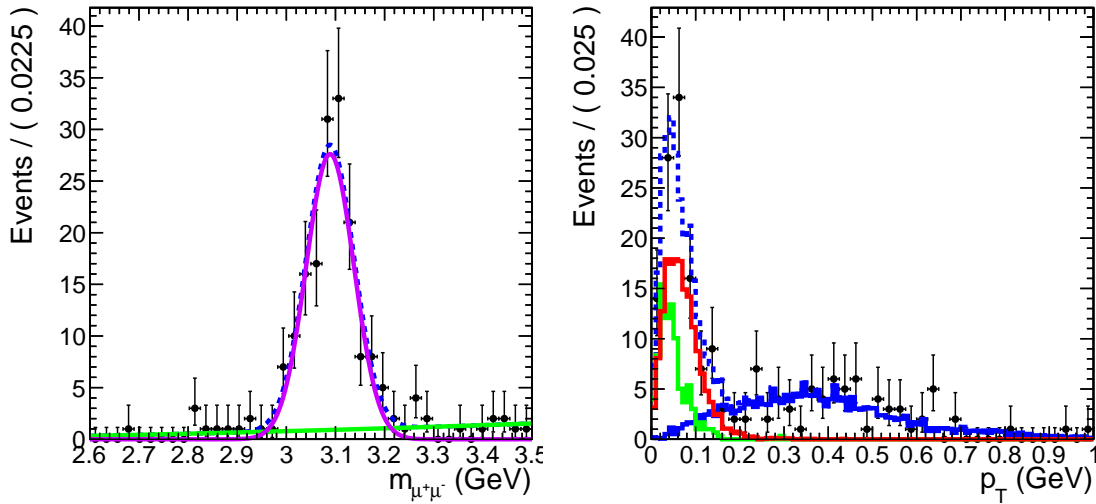


Figure 1.11: Simultaneous fit to the mass and p_T spectra.

359 Fig. ?? shows the confidence contours for nCo and $nGamma$ from the simultaneous fit in
 360 Fig. ?. The slope of the confidence contours in Fig. ?? is noticeably than in Fig. ?. The contours
 361 for the simultaneous fit are also reduced compared to Fig. ?? with widths in nCo and $nGamma$

362 similar to those expected from Poisson statistics. From the simultaneous fit, reasonable statistical
 363 errors were obtained along with the yields for the three processes.

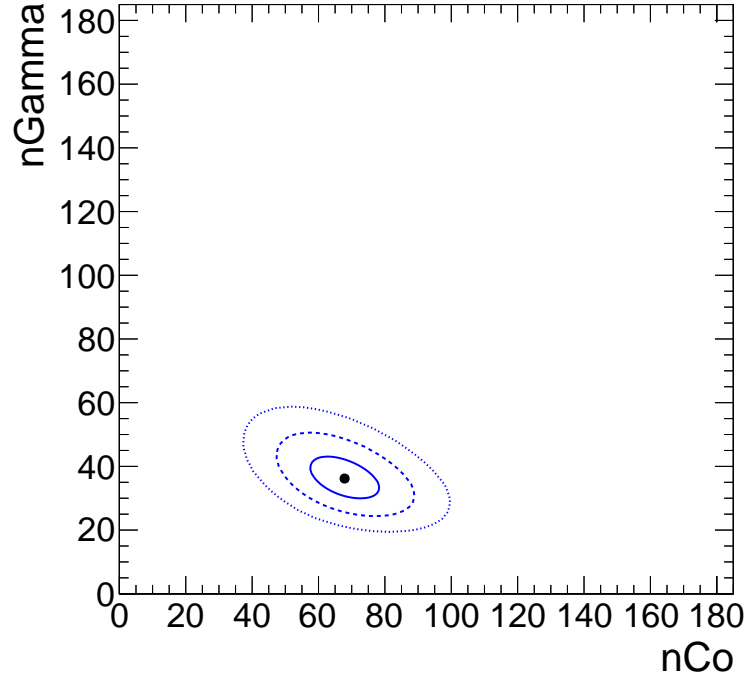


Figure 1.12: 68%, 95%, and 99% confidence contours from the simultaneous fit.

364 1.6 Efficiency determination

365 Each step of the triggering, event selection, and analysis has an associated efficiency that must be
 366 accounted for in the measurement of the J/ψ cross section. The ZDC trigger efficiency, the muon
 367 trigger efficiency, and the muon reconstruction efficiency are the two most significant contributors
 368 to the total efficiency measurement. The efficiency of the pixel track requirement, and the veto on
 369 activity in the BSCs from the trigger are also estimated but found to be consistent with fully effi-
 370 cient. The following section explains how each of these efficiencies were measured with a special
 371 emphasis on the ZDC trigger efficiency and the muon trigger and reconstruction efficiencies.

1.6.1 Muon efficiencies

The muon efficiencies were measured using a combination of MC and data based methods. The MC based measurement accounts for the detector acceptance and the efficiency of the muon quality cuts discussed in Section ???. The trigger efficiencies were measured in data using the tag and probe method [?], which is discussed below.

CMS has a limited acceptance for J/ψ s, particularly in the case of J/ψ s with low momentum like those produced in UPC events. To measure the acceptance of CMS for J/ψ s, reconstructed dimuon candidates were considered detectable if both reconstructed muon daughters fell into a detectability region in p_T and η . The muon detectability region was defined using the coherent J/ψ events obtained from STARlight. The efficiency for reconstructing single muons ϵ_{reco}^μ is defined by $\epsilon_{reco}^\mu = \frac{N_{reco}^\mu}{N_{gen}^\mu}$, where N_{reco}^μ is the number reconstructed muons obtained after the full CMS detector simulation and that passed the standard muon quality cuts, and N_{gen}^μ is the number of generated muons from STARlight. Fig. ?? shows the efficiency for reconstructing single muons from coher-

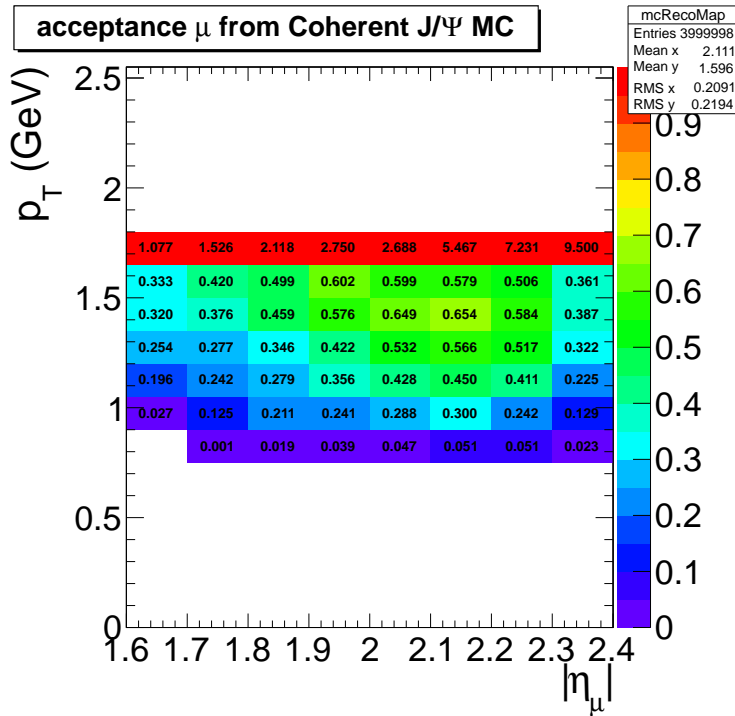


Figure 1.13: Muon daughter detectability from coherent J/ψ

ent J/ψ events. To avoid the edges of the detectors acceptance, all reconstructed muons that fall

into a $(p_T, |\eta|)$ bin that has an efficiency less than 20% were rejected. This condition defines the detectability region. The acceptance for reconstructing dimuons was calculated from MC using the following formula:

$$A = \frac{N_{det}(|y|, p_T)}{N_{gen}(|y|, p_T)}, \quad (1.2)$$

where N_{det} is the number of reconstructed dimuons where both daughters fall into the detectability region, and N_{gen} is the number of generated dimuons. From Eq. ??, the acceptance for J/ψ was calculated as a function of $|y|$, and p_T (see Fig. ??).

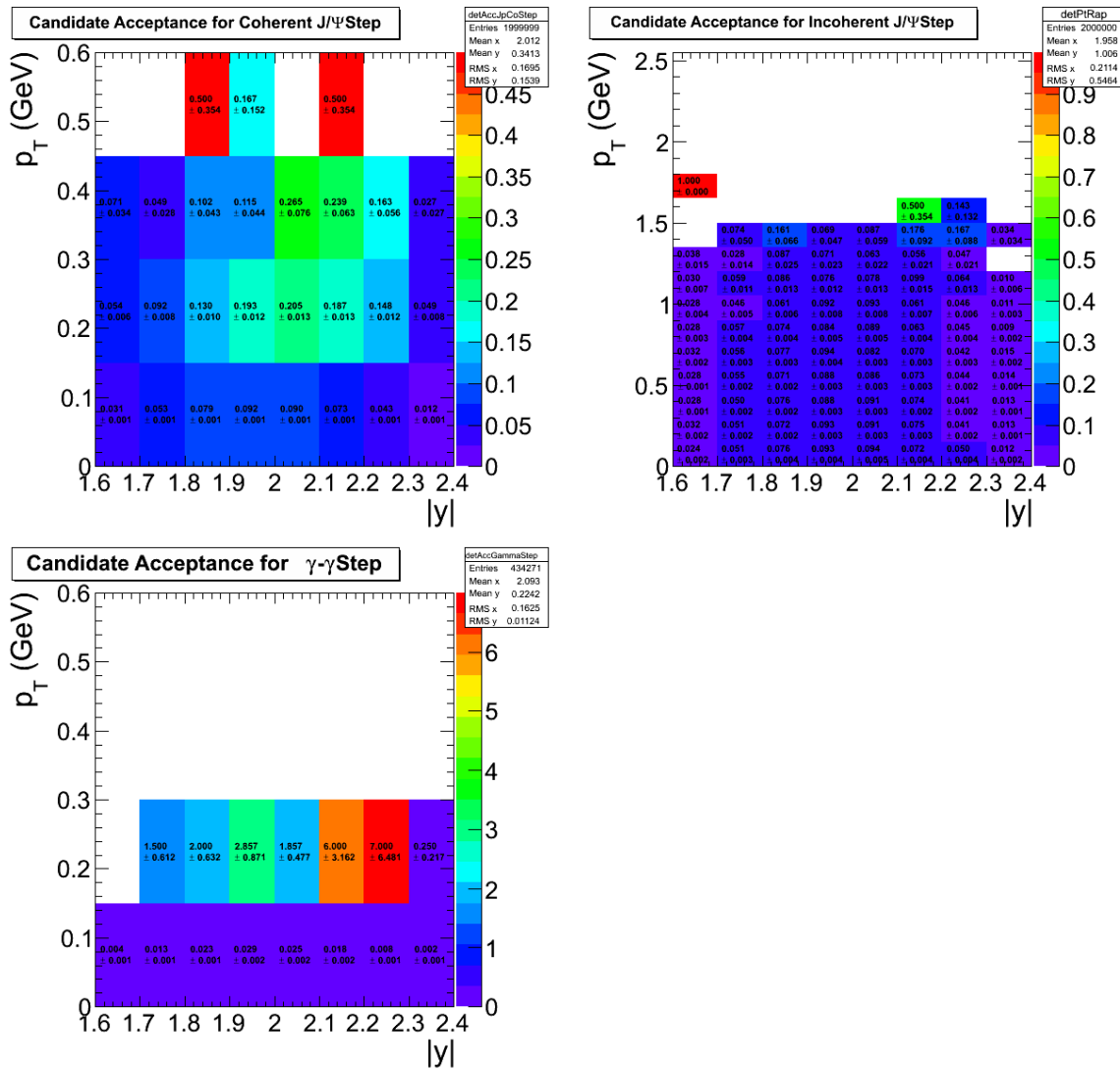


Figure 1.14: Dimuon acceptance from coherent J/ψ (top left), incoherent J/ψ (top right), and photon-photon interactions (lower).

The "tag and probe method" is a data driven approach used to measure the trigger efficiency of the muon daughters from J/ψ decays. In this method there are three categories of daughter muons. *Tag muons* are high quality muons. *Passing probes* are reconstructed muons that match the muon trigger, while *failing probes* do not. Each dimuon will have one daughter classified as a tag and the other as a probe. From here three invariant mass histograms are studied. One histogram is created from all pairs. The second comes from pairs where the probe is a passing probe. The last histogram comes from pairs where the probe fails to fulfill the trigger, *i.e.* the probe is a failing probe. By matching the tag to the trigger, the probe is unbiased by the trigger and the efficiency can be measured by fitting the three mass histograms.

Because the trigger efficiency depends on the p_T and $|\eta|$ of the muon, one set of three histograms for each $(p_T, |\eta|)$ bin of the probe is created. To extract the single muon trigger efficiency ϵ_{trig}^μ , each set of invariant mass histograms were simultaneously fit. The signal was fitted using a Crystal Ball function, and the background was fitted to an exponential. The Crystal Ball parameters were simultaneously fitted to all three histograms. The exponential function was fitted to the failing and passing probe histograms separately. Because the background shapes are in principle different for the two samples, the efficiency is driven by this difference.

Fig. ?? shows the fit of the three sets of pairs. This fit was done for each bin of the probes p_T

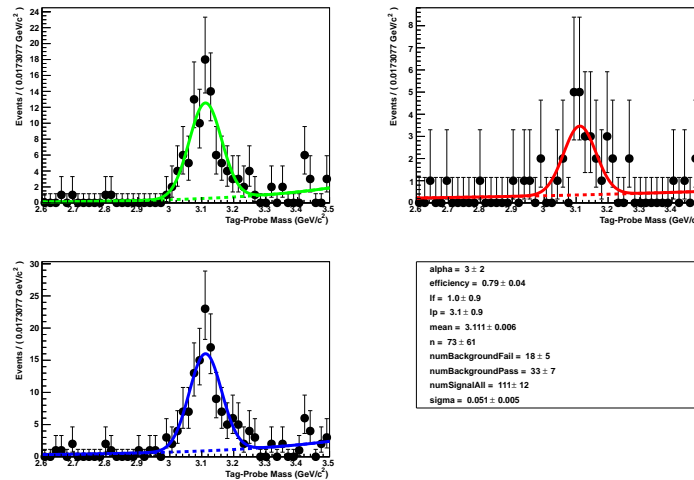


Figure 1.15: Fits to tag and probe pairs in the J/ψ mass region for pairs with a probe $2 < |\eta| < 2.2$ and $1.55 < p_T < 1.8$ GeV.

and η . The efficiency from the fits in each bin are [shown](#) in Fig. ??.

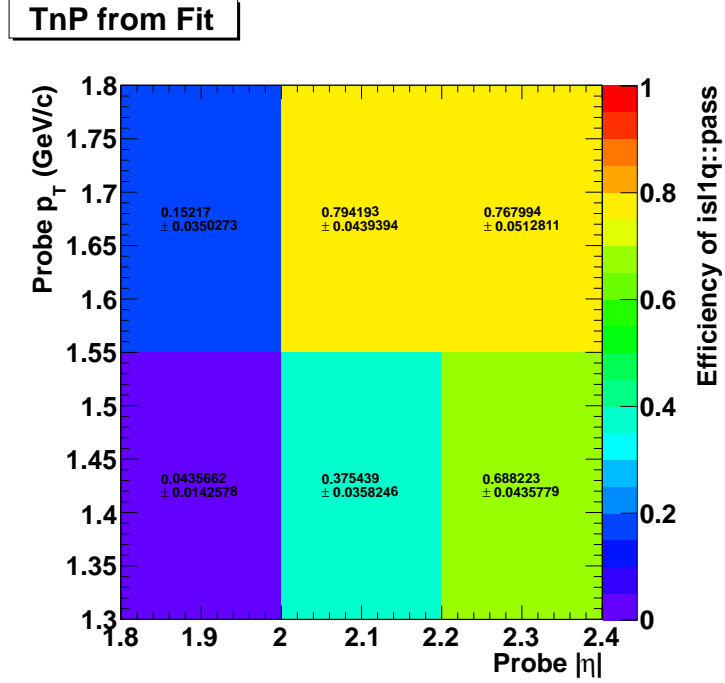


Figure 1.16: Muon trigger efficiencies in p_T and η bins from the tag and probe method.

409

410 The dimuon trigger efficiency $\epsilon_{trigger}^{dimuon}$ was calculated from the single muon efficiencies using
 411 the following equation:

$$\epsilon_{trigger}^{dimuon} = 1 - (1 - \epsilon_{trigger}^{\mu_1})(1 - \epsilon_{trigger}^{\mu_2}), \quad (1.3)$$

412 where $\epsilon_{trigger}^{\mu_1}$ is the tag and probe efficiency of the first dimuon daughter, and $\epsilon_{trigger}^{\mu_2}$ is the effi-
 413 ciency of the second muon daughter. In Eq. ?? the probability of at least one daughter firing the
 414 trigger is calculated by subtracting one from the probability that neither daughter fires the trigger,
 415 thus giving the dimuon trigger efficiency.

416 The average dimuon trigger efficiency for each dimuon ($p_T, |y|$) bin was calculated by averag-
 417 ing the efficiency of dimuon candidates in each bin. The dimuon trigger efficiency ranges from
 418 $\approx 50\%$ to 87% . As expected the J/ψ trigger efficiency increase with rapidity since the longitu-
 419 dinal momentum of the J/ψ is given $p_z = M_{J/\psi} \cdot \sinh(y)$. Thus J/ψ mesons at forward rapidity
 420 distribute more momentum to their daughter muons which therefore have a greater chance of

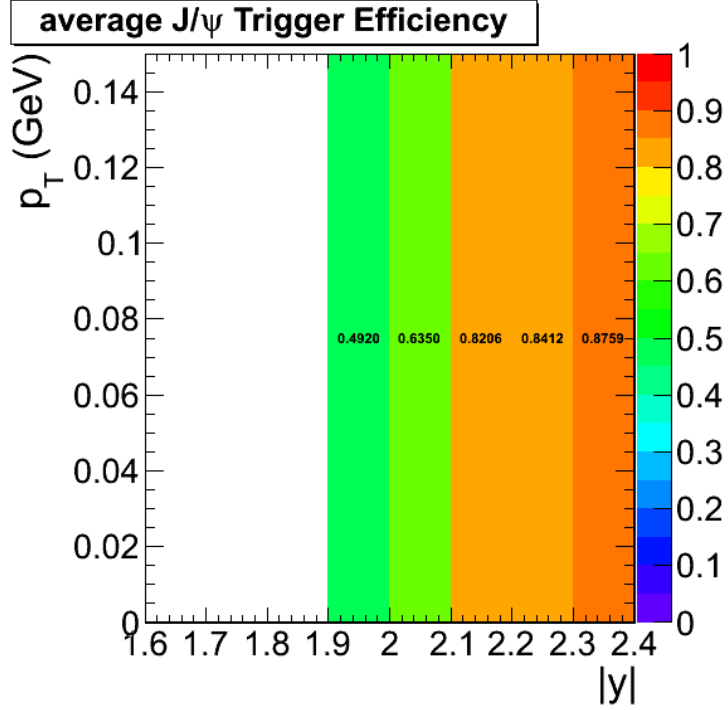


Figure 1.17: The trigger efficiency from tag and probe averaged over candidates in each $(p_T, |y|)$ bin.

punching through into the muon chamber. The average trigger efficiency was multiplied by the acceptance and reconstruction efficiency from the MC to produce a total factor for both efficiency and acceptance.

The total combined efficiency and acceptance factor coherent J/ψ between $2.0 \leq |y| \leq 2.2$ was found to be $\approx 5\%$. The acceptance factor of roughly 7% from the MC was found to be the main contributor to the total efficiency. The interplay of the polarization of the J/ψ and the material in detector drive down the efficiency by creating an effective momentum threshold for detection (see Section ??). The reconstruction efficiency of the daughters range between 20%-60% for muons in the defined detectability range. The trigger efficiency for the detectable muons ranges from 30%-80% depending on p_T .

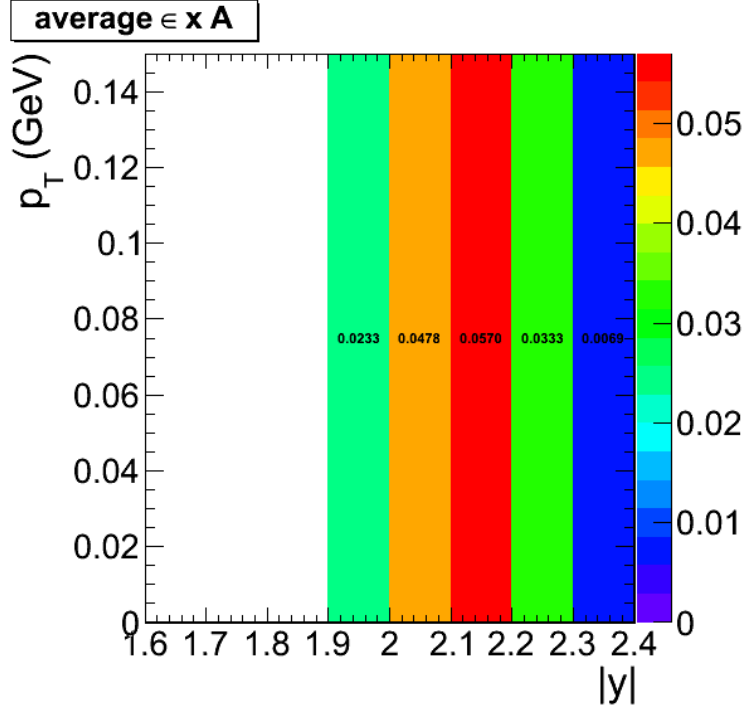


Figure 1.18: The acceptance times averaged trigger efficiency from tag and probe.

1.6.2 ZDC trigger efficiency

As discussed in Section ??, the trigger labeled "L1ZDCOr and Pixel Track" in Table ?? was used to estimate the measure the ZDC trigger efficiency. This trigger required either a ZDC^+ or ZDC^- trigger, together with at least one pixel track. The veto on the BSC minimum bias trigger, as in the physics triggers, was applied offline. The BSC veto excludes events where BSCs from both sides of the interaction point are above threshold. This trigger was used in order to collect the most inclusive possible sample without using the minimum bias triggers designed to collect hadronic interactions.

This ZDC triggered sample suffers from a trigger bias. For example, a sample triggered by ZDC^+ would always produce a ZDC^+ trigger efficiency of one. To avoid this, a similar technique to tag and probe was used. Each event is either tagged as triggered by ZDC^+ or triggered by the ZDC^- . The ZDC^+ trigger efficiency is measured from the ZDC^- tagged sample, and vice versa.

To estimate the efficiency, the number of events with energy in ZDC^+ greater than the single neutron threshold, N_{events} , were measured. From this set of events, the number of events that also

	ZDC Side	Reco Method	N_{events}	N_{trig}	ϵ_{ZDC}
zo	ZDC ⁺	1	72946	71688	0.982 ± 0.005
	ZDC ⁺	2	73028	71706	0.9819 ± 0.005
	ZDC ⁻	1	76137	71786	0.9429 ± 0.005
	ZDC ⁻	2	76132	71859	0.9439 ± 0.005

Table 1.5: ZDC trigger efficiencies for ZDC reconstruction method 1 and 2

445 fire the ZDC⁺ was measured. The ratio between the number of single neutron events that fired
 446 the trigger and all single neutron events was taken as the estimate of trigger efficiency. The same
 447 procedure was applied for each side of the ZDC. The trigger efficiency was found to be 98% for
 448 ZDC⁻ and 94% for ZDC⁺.

449 1.7 Systematic checks

450 Table ?? shows the systematic errors that were estimated. The method used to separate the coherent
 451 from the photon-photon process is the most dominant error. The ZDC reconstruction method used
 452 to estimate the neutron thresholds is the next most dominant, followed by the method used to
 453 estimate the HF noise threshold.

systematic	uncertainty in %
Template fit normalized	+9.5% -12%
ZDC reconstruction	2.9%
ZDC trigger efficiency	2.2%
HF noise threshold	+1.3% -3.4%
MC acceptance	1.1%
Total systematic	8.1%

Table 1.6: Summary of systematic uncertainties

454 1.7.1 HF noise threshold

455 The way in which the HF noise distribution is measured effects the event selection and therefore
 456 the final candidate yeild. This cut plays a significant role in rejecting hadronic events. In Table ??

the importance of cutting on HF noise is evident. The HF noise cut rejects a nearly 1/5 of the remaining events. The systematic uncertainties on the HF noise requirement is important for this reason.

The most fine grained data from the HF detectors are called RecHits. There is one RecHit per phototube on HF. The RecHit signal is calibrated in GeV and no noise subtraction is done. The CaloTowers are formed from geometrical groups of RecHits. They are the first stage of the CMS jet trigger and perform some noise suppression.

The default HF noise cut required that the maximum RecHit energy from both HF+ and HF- be less than 3.85 GeV. This cut was designed to accept 99% of the noise events, see Fig. ???. The stability of this cut was tested by

1. Summing CaloTowers instead of RecHits
2. Making separate cuts on HF- and HF+
3. Tightening the threshold so that only 98% or 97% noise events passed the cut.

Table ??? shows the noise thresholds for RecHits and CaloTowers for both the combined HF+ and HF- calorimeters and the individual calorimeters when 99% of noise events are accepted. Table ??? compares the threshold for the cases when 99%, 98% and 97% of noise events are accepted. The number of J/ψ events remaining after these cuts is shown in EXPANDED TABLE. The efficiency corrected numbers are also shown. The fractional systematic error is then estimated by finding the maximum and minimum deviation from the default method. The systematic uncertainty from this method is calculated to be +1.3% -3.4%.

Object type	HF (GeV)	HF ⁻ (GeV)	HF ⁺ (GeV)
RecHits	3.85	3.25	3.45
CaloTowers	4.25	3.25	3.75

Table 1.7: HF noise thresholds for various noise measurement methods.

Object type	Combined HF threshold	Two-sided thresholds
RecHits	298	290
CaloTowers	302	288

Table 1.8: Candidate yields below 1.05 GeV p_T for various HF noise cuts.

Table 1.9: Values of the energy cuts for the HF calorimeter for RecHit and CaloTower in GeV.

%	E_{RecHit} GeV	$E_{CaloTower}$ GeV
99	3.85	4.25
98	3.25	3.75
97	2.95	3.25

Table 1.10: Number of dimuon candidates with $p_T < 1.05$ when changing HF calorimeter cuts for RecHit and CaloTower.

%	RecHit cut	CaloTower cut
99	298	302
98	287	294
97	284	280

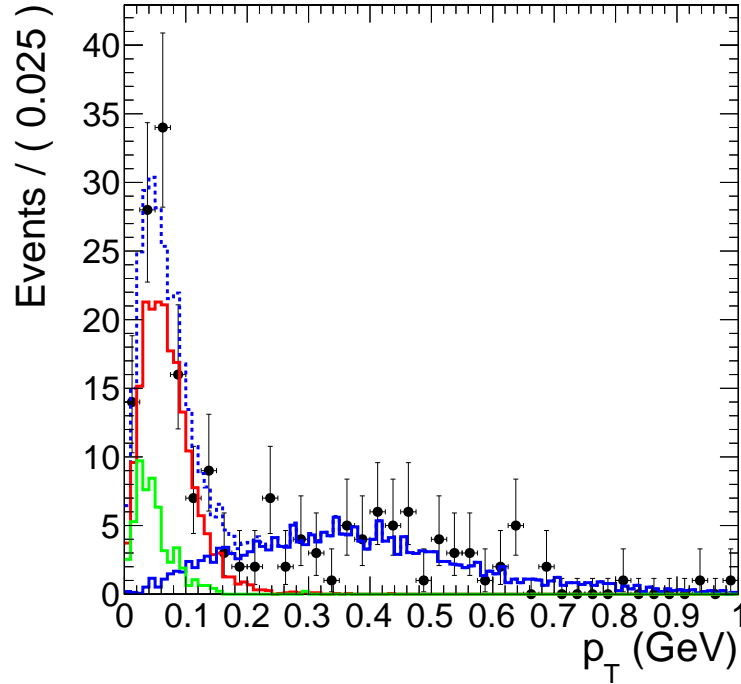


Figure 1.19: Coherent, incoherent, and photon-photon process p_T template fit to data.

1.7.2 Template fit normalization

The p_T template fit depends on the functions chosen for the fit to the mass distribution. As described in Section ??, the similarity of the of the p_T distribution for the coherent and photon-photon process make the contributions from the two process difficult to separate from the p_T distribution alone. The mass distribution was used to distinguish between these two processes. In turn, the p_T becomes dependent on the mass fit.

The systematic uncertainty due to the choose of functions used to fit the mass distribution was estimated by varying the signal and background functions. The contribution to the background from the mass fit was used to fix the contribution from the photon-photon process in the p_T template fit. Two functions were used to describe the signal, a Gaussian, and a Crystal ball function. The background was fit to a linear function, a 2nd order polynomial, and a 2nd order Cheby-Chev polynomial. The resulting variation on the coherent contribution was used to as an estimate of this systematic effect.

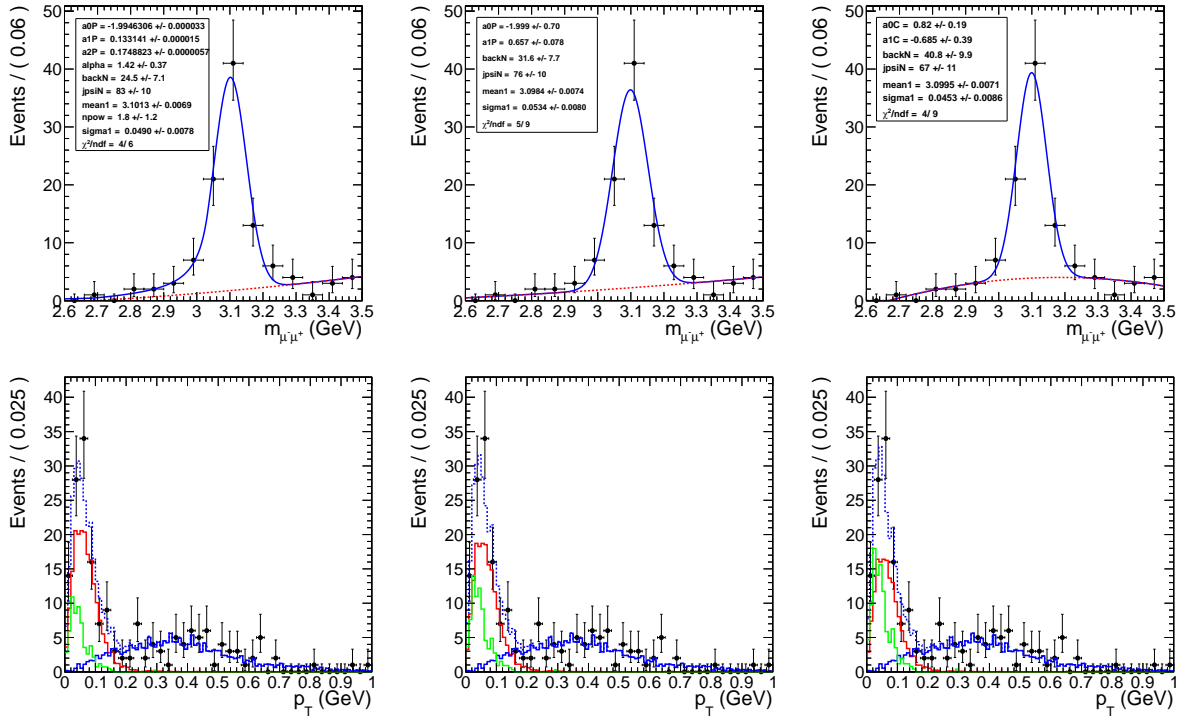


Figure 1.20: Various mass distribution fits and the corresponding p_T template fit.

Moving from left to right in Fig ??, the contribution from the photon process increases. The χ^2 pre degree of freedom is similar between the three fits indicating a similar goodness of fit. On this basis, neither fit is preferred. The left most fit uses a Crystal Ball function to account for the radiative decay of the final state daughters of the J/ψ . The low mass exponential portion however picks up background events and overestimates the J/ψ contribution. The right most plot fits the background to a 2nd order Cheby-Chev polynomial. Because the Cheby-Chev peaks just below the J/ψ peak, this fit overestimates the background and in turn underestimates the signal contribution. The Gaussian fit with a linear background however does a reasonable job of fitting both the background and the signal.

From these three fits an upper and lower bound of the systematics due the choice of fit functions was estimated. The difference between the Gaussian-Linear fit and the Crystal Ball-polynomial fit was taken as an upper bound. The difference between the Gaussian-Linear fit and the Gaussian-Cheby-Chev fit was taken as a lower bound. The overall systematic uncertainty due to the choose of mass fit functions is found to be +9.5% -12%.

1.7.3 Mass fit

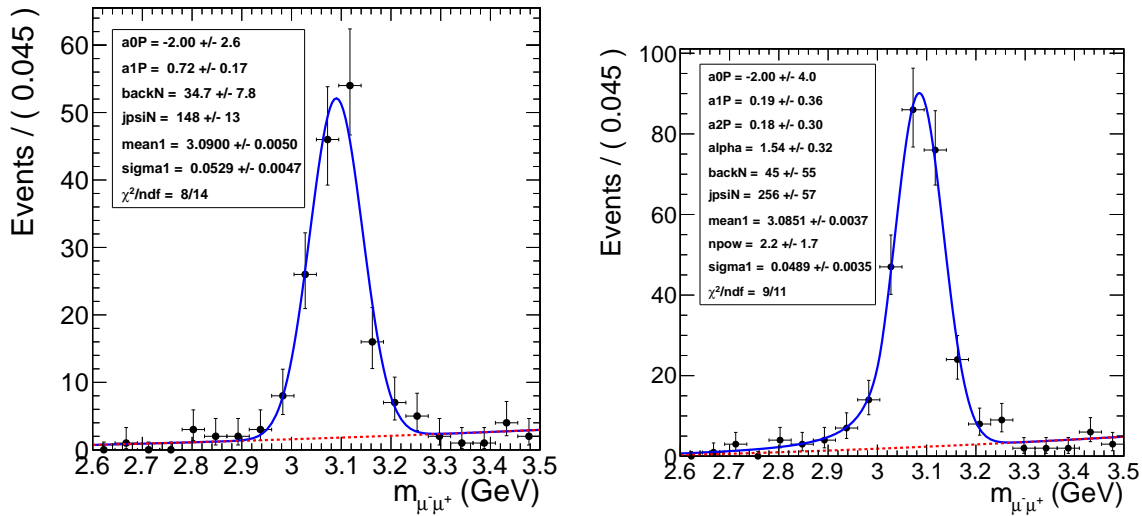


Figure 1.21: Mass fit to J/ψ using Gaussian (Left) and Crystal Ball (Right) for the signal and a polynomial for the background

Fig. ?? demonstrates the small dependence the raw J/ψ yield has on the fitting function. Both fit functions agree well, with reduced χ^2 values below one. The Crystal ball fit give an upper estimate for the J/ψ yield. The Gaussian fit gives an lower estimate. The main difference comes from the lower mass tails. In the Crystal ball fit the lower tail is considered to be signal due to shifting of the mass spectrum to lower mass due to radiation from the final state muons. In the Gaussian fit the lower mass tail is considered to be background and the signal is sharper.

As check on the simultaneous p_T and mass fit, the mass fit is done using mass templates from STARlight.

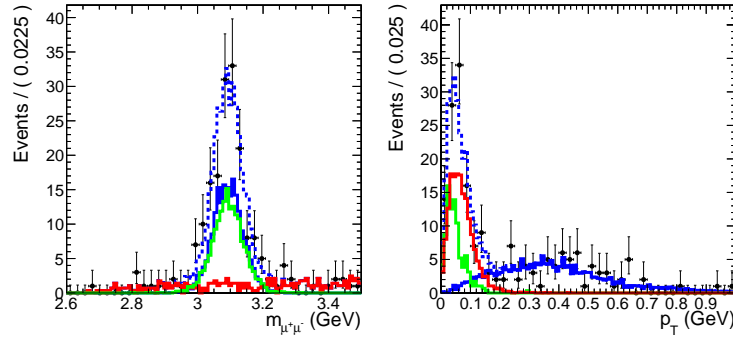


Figure 1.22: Simultaneous fit to the mass and p_T using mass templates for the mass fit.

1.7.4 MC acceptance

The MC derived acceptance correction factors depend on the input physics generator. The underlying p_T distribution was assumed to be correctly described by STARlight for the coherent cross section measurement. To estimate the effect of changing the underlying p_T distribution on the acceptance measured from the MC, the incoherent sample was used to correct the coherent yield. By using the broader p_T distribution of the incoherent process, an estimate of acceptance measurements dependence on the assumed shape of the p_T distribution was obtained. The systematic uncertainty due to the dependence of the acceptance correction on the p_T distribution of the input physics generator was estimated by the difference between the correction factors from the coherent and incoherent MC samples. Half the difference was used as the estimate and was found to be

523 1.1%.

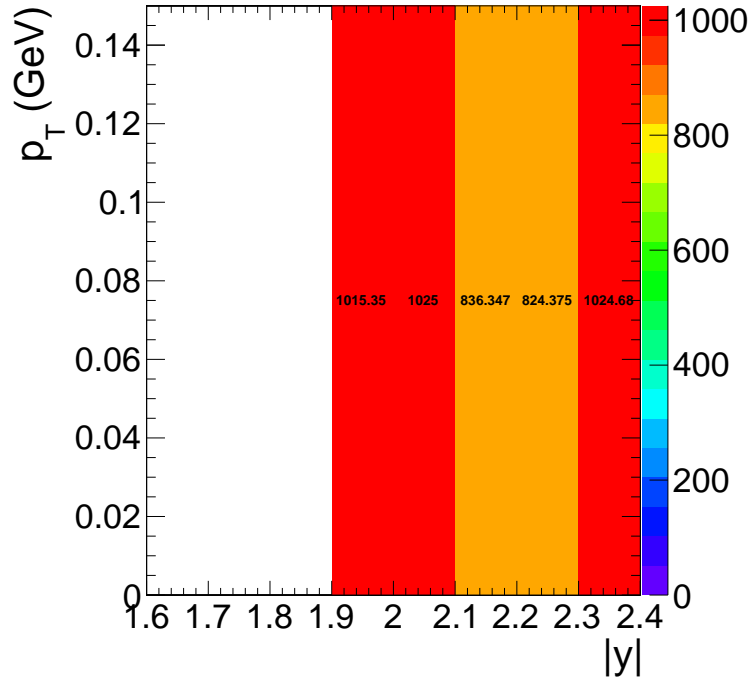


Figure 1.23: Yields corrected by the MC incoherent acceptance map.

524 The effect of polarization was estimated by correcting by the acceptance for an unpolarized
 525 J/ψ sample.

526 1.7.5 ZDC reconstruction

527 An additional method for estimating the ZDC neutron thresholds was used to estimate the sys-
 528 tematic errors on the threshold measurements. This additional method, used in previous ZDC
 529 measurements, differs in the way the signal time slices are used to calculate the signal from each
 530 channel. In the standard method, the signal is taken from the sum of time slices 4, 5, and 6. To
 531 estimate the event by event noise pedestal the sum of time slice 1 and 2 are used. The signal for
 532 an individual ZDC channel is then calculated as the sum of the signal time slices minus the sum
 533 of the noise time slices weighted by a factor of 3/2 to account for the differing number of noise
 534 versus signal time slices. The advantage of the standard method is that by using multiple signal
 535 and noise time slices the signal and noise are effectively averaged reducing time slice to time slice

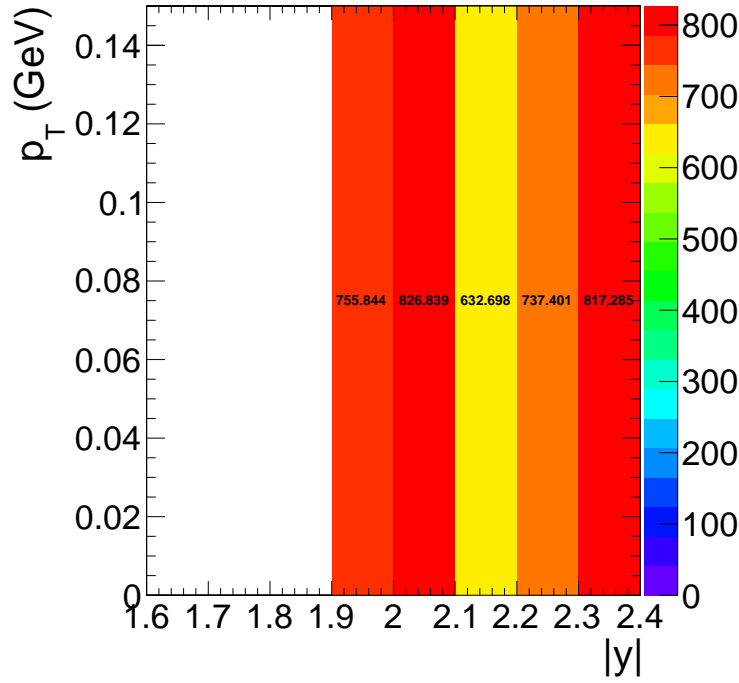


Figure 1.24: Yields corrected by an unpolarized J/ψ sample.

fluctuations. However, by using time slices 1 and 2 for measuring the noise, the noise can only be measured half the time due to unmeasurable negative fluctuations of the dominant low frequency component of the noise.

As in the new method described in Section ??, the standard method combines the channels to create a signal measurement from the whole of each side of the ZDC, one measurement for ZDC^+ , and one for ZDC^- . The noise subtracted signal from each of the HAD channels are added together. Then the EM section channels are summed. The EM section is weighted by a factor of 0.1 as in the new method. After the weighting the EM and HAD channels are added to each to create one measurement for ZDC^+ and another measurement for ZDC^- .

Fig. ?? shows the spectra for ZDC^+ and ZDC^- using the standard method. The same fit used for the new method is applied to standard method. As in the new method, the single neutron threshold is set to 2σ below the mean from the fit to the one neutron peak. The multi-neutron threshold was set to 2σ above the one neutron peak.

The systematic uncertainty due to the ZDC reconstruction method are estimated from the dif-

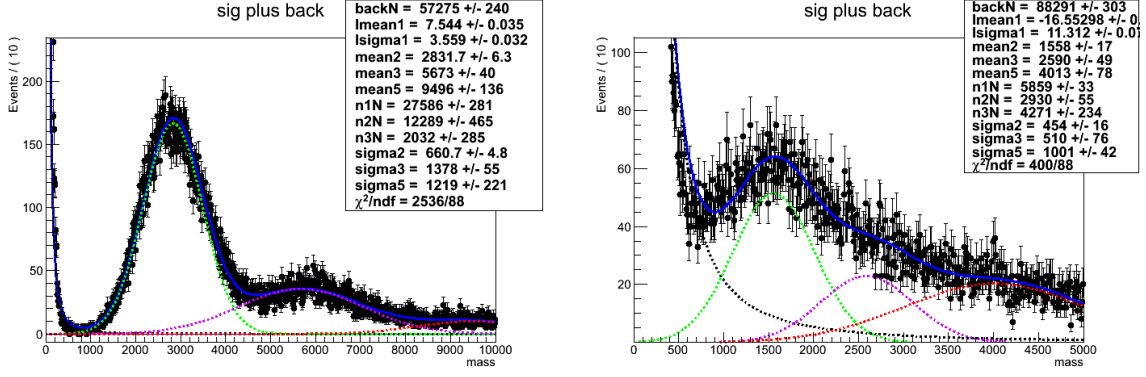


Figure 1.25: Fit to charge spectrum from ZDC⁻ (left) and ZDC⁺ (right) using the standard reconstruction method

ference between the UPC J/ ψ candidate yields. Both the reconstruction method and thresholds were changed to calculate the effect of the reconstruction method. The yields for the new and standard ZDC reconstruction method in the Xn0n break up were found to be 298 and 315 respectively. Half the difference between the two methods was used as an estimated of the systematic uncertainty. The systematic uncertainty due to the ZDC reconstruction method was found to be 2.9%.

1.7.6 ZDC trigger efficiency

The ZDC trigger efficiency measurement is sensitive to the underlying neutron distribution. The more neutrons that high the ZDC the higher the trigger efficiency will be. To estimate the effect the input sample has on the efficiency, the ZDC trigger efficiency was measured from five different samples. The Table ?? shows the results from the five samples. Both the new and standard ZDC reconstruction methods are shown for comparison.

The amount of electronic noise in the sample also effects the measurement. The more noise sits below the one neutron peak, the worse the efficiency is. In Table ??, the Zero Bias sample compared the Zero Bias sample with the timing cuts the described in the previous section shows a significant increase in efficiency in the sample with reduced noise. The same increase is seen when comparing the ZDC triggered sample with the ZDC triggered sample that also requires a

ZDC Side	Reco Method	N_{events}	N_{trig}	ϵ_{ZDC}
(ZDC ⁺ or ZDC ⁻) and 1 pixel track				
ZDC ⁻	1	72946	71688	0.982 ± 0.005
ZDC ⁻	2	73028	71706	0.9819 ± 0.005
ZDC ⁺	1	76137	71786	0.9429 ± 0.005
ZDC ⁺	2	76132	71859	0.9439 ± 0.005
(ZDC ⁻ or ZDC ⁺), 1 pixel track, and L1 EG trigger				
ZDC ⁻	1	613758	602123	0.9810 ± 0.0018
ZDC ⁻	2	614014	601863	0.9802 ± 0.0018
ZDC ⁺	1	643905	602671	0.9360 ± 0.0017
ZDC ⁺	2	647888	603089	0.9309 ± 0.0017
(ZDC ⁻ or ZDC ⁺), 1 pixel track, and L1 Muon trigger				
ZDC ⁻	1	65466	63376	0.9681 ± 0.0054
ZDC ⁻	2	65543	63358	0.9667 ± 0.0054
ZDC ⁺	1	71929	63512	0.8830 ± 0.0048
ZDC ⁺	2	72932	63582	0.8718 ± 0.0047
Zero Bias with ZDC timing cuts				
ZDC ⁻	1	88676	84429	0.9521 ± 0.0046
ZDC ⁻	2	88480	84202	0.9517 ± 0.0046
ZDC ⁺	1	59878	54728	0.9140 ± 0.0054
ZDC ⁺	2	60467	54733	0.9052 ± 0.0053
(ZDC ⁻ or ZDC ⁺)				
ZDC ⁻	1	30986	30333	0.9789 ± 0.0079
ZDC ⁻	2	31029	30339	0.9778 ± 0.0079
ZDC ⁺	1	39178	30164	0.7699 ± 0.0059
ZDC ⁺	2	35703	30443	0.8527 ± 0.0067
Zero Bias				
ZDC ⁻	1	109967	101598	0.9239 ± 0.0040
ZDC ⁻	2	110230	101561	0.9214 ± 0.0040
ZDC ⁺	1	253241	86660	0.3422 ± 0.0013
ZDC ⁺	2	156336	87401	0.5591 ± 0.0024

Table 1.11: ZDC trigger efficiencies for ZDC reconstruction method 1 and 2 for different trigger samples

pixel track. The effect of the electronic noise is also present in the difference seen in using the two methods. As seen in Fig. ??, the new reconstruction method shows better separation of the one neutron peak from the electronic noise, in particular in ZDC^+ where the signal gain is lower. For this reason, the Zero Bias data, which contains that largest contribution from electronic noise, shows the most separation between the two methods and give the lowest estimate for the ZDC trigger efficiency.

The systematic uncertainty due to the uncertainty in the underlying distribution was estimated by calculating the standard deviation of the least extreme values from Table ?. Any value greater than three standard deviations from the mean was thrown out.

1.7.7 ZDC reconstruction method comparison

The new method relative to the standard method separates low signal from the noise more effectively for both sides of the ZDC. This is particularly important for ZDC^+ where the 1st HAD section had a lower gain than the other sections. The ZDC^+ and ZDC^- signals near the one neutron peak using the standard and new reconstruction methods were plotted for comparison in Fig. ?. In Fig. ??, the shrinking of width of the noise peak around zero in the new method versus the old

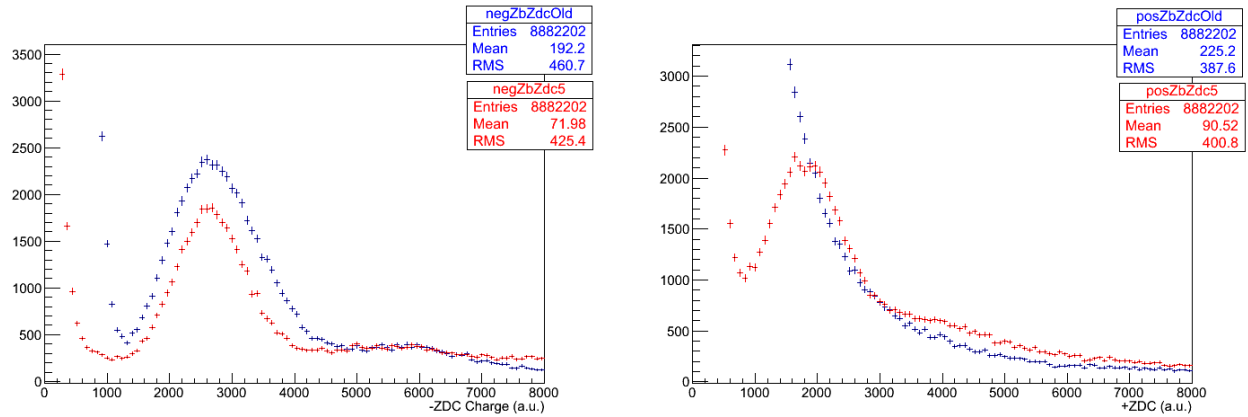


Figure 1.26: Comparison of the **new** ZDC reconstruction method and the **standard** method for ZDC^- (left) and ZDC^+ (right).

method is apparent for both ZDC^+ and ZDC^- . For the standard method no single neutron peak is resolved in ZDC^+ , whereas the single neutron peak is resolved using the new method.

Timing cuts were applied to enhance the signal relative to the background in order to resolve the one neutron peak in ZDC^+ using the standard method. Because the products of the collision are synced with time slice 4, noise can be rejected by selecting channels where the maximum signal falls into time slice 4. The noise will have no preferred time slice (see Fig. ??). Using this fact, signal can be preferably selected by requiring that the hadronic channels of the ZDC have a peak signal in the fourth time slice. Through these timing cuts the single neutron peak was recovered using the standard reconstruction for ZDC^+ .

To examine the effectiveness of the timing cuts, event by event noise subtraction was removed from the standard reconstruction. The signal from each channel was taken from time slices 4,5, and 6 with out subtracting 1 and 2. The signal spectrum from ZDC^- was then plotted with the result shown in Fig. ?. As each additional hadronic channel is required to have a maximum signal in

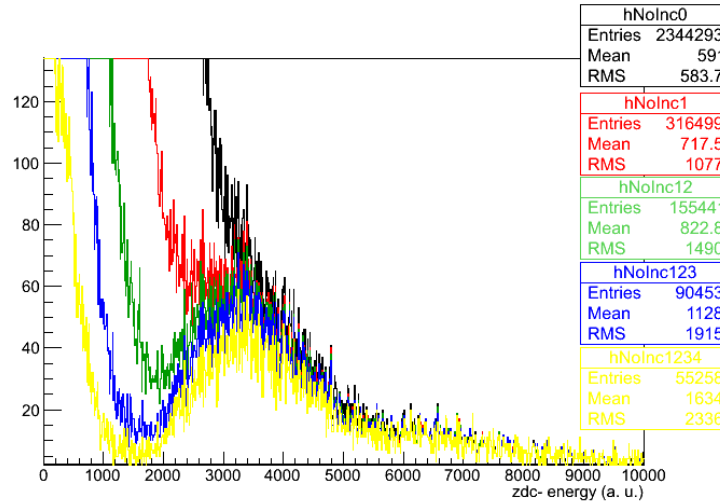


Figure 1.27: Effects of requiring in-time signal in successively more ZDC hadronic channels, no timing, at least **one**, at least **two**, at least **three**, and all **four** HAD channels have a maximum signal in the fourth time slice.

the fourth time slice, the single neutron peak emerges. Fig. ?? demonstrates that the single neutron peak can be recovered from the noise using timing cuts alone.

Using the standard noise subtraction method, the same signal that emerges from the timing cuts alone appear without timing cuts. Fig. ?? confirms that both noise subtraction and the timing requirement produce the same signal. This gives confidence that the signal is not an artifact of

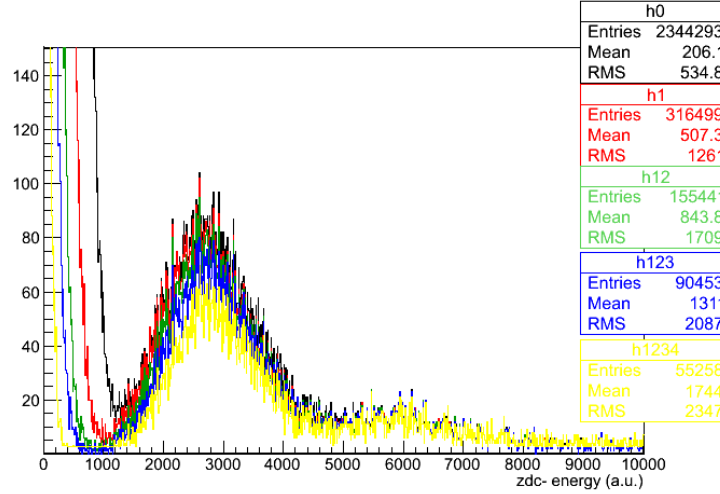


Figure 1.28: Effect of ZDC signal timing requirements after noise subtraction.

either cut, but the true neutron signal.

Fig. ?? and Fig. ?? demonstrate the consistence of the using timing cuts and noise subtraction to enhance the signal neutron peak. Fig. ?? confirms the legitimacy of the timing requirement method in ZDC^- by showing the that the same signal emerges from the noise subtraction method as the timing method. Fig. ?? demonstrates the corresponds between the new noise subtraction method and the standard method on in ZDC^- where signal is better separated from the electronic noise. This allows for confidence that the signal seen in ZDC^+ using the new method is the one neutron peak.

1.7.8 Tag and probe

The main purpose for fitting the mass spectra to estimate the efficiency is to separate the background from true signal. The background may not have the same efficiency as the signal, so separating the two is important if this is the case. In the tag and probe fit the signal peak from the J/ψ resonance is fit to the probes, passing probes, and failing probes alike (see Fig. ??). The signal shape, if from the same physical signal, will be identical in each of the three distributions. The background is for the passing and failing probes is fit using different parameters for the background because the background may come from different physical processes than the signal or

non-physical sources like combinatorial backgrounds or misidentified fake particles. When the background comes from sources other than the physical signal, the background may give an efficiency estimate that is lower than the signal.

The trigger efficiency measured by the tag and probe method depend on the fitting functions use to estimate the background and signal contributions. Depending on what functions is used to fit the spectra, the amount of amount of background can be over or underestimated and effect the efficiency measurement. To estimate this effect, the tag and probe efficiencies were additionally measured by counting probes in the J/ψ mass window. The whole mass window is used to estimate the efficiency including all the events from the mass side bands. In this way, a worst case scenario estimate is given where all background events are included as signal.

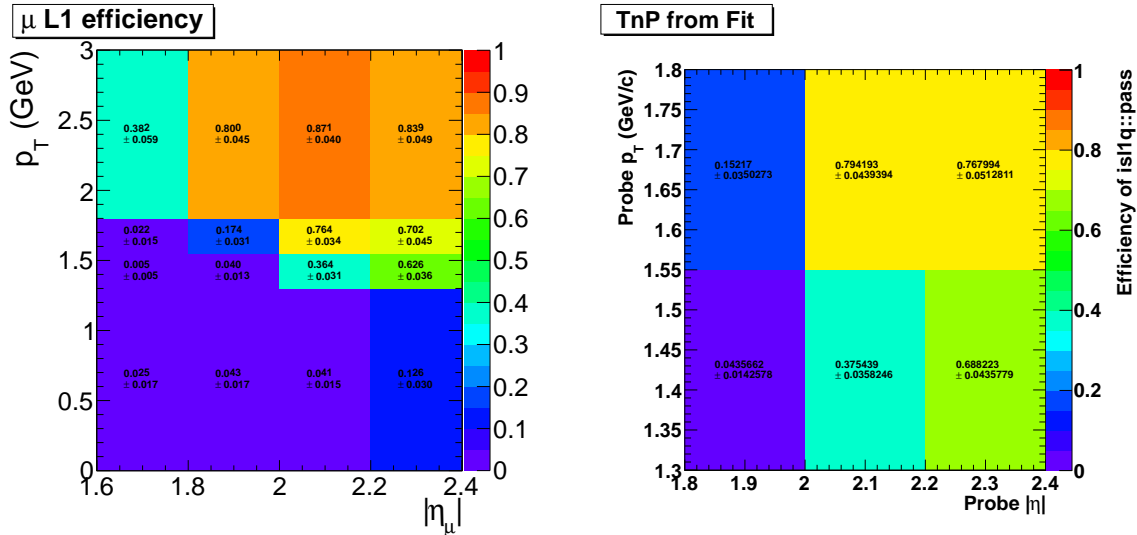


Figure 1.29: Tag and probe trigger efficiencies from counting (left) compared to fitting (right)

From Fig. ?? it is apparent that the choice of fit function and therefore the amount of background from the mass side bands is included in the signal measurement has very little effect on the tag and probe efficiency measurement. The small effect of including the side bands is due to the side bands being comprised mostly of photon-photon events. Because this background is neither decays from other particles like pions nor is it non-physical background like combinatorics, the efficiency for muons from the sidebands are nearly identical to J/ψ signal. The photon-photon process directly produces two muons just like the J/ψ , therefore efficiency estimated from the side

bands has little effect on the measurement because of this similarity. The counting and fitting trigger efficiency measurements agree within statistical uncertainties, so this uncertainty was taken to be negligible.

1.7.9 MC vs Data compairson

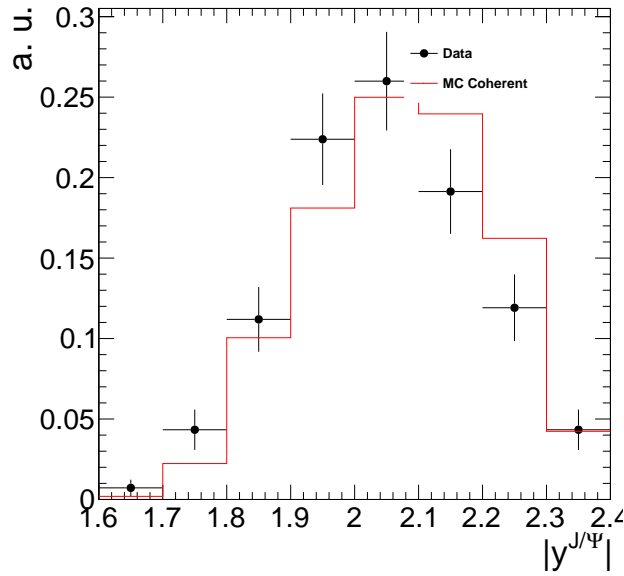


Figure 1.30: Comparison of the of the dimuon rapidity distributions between coherent MC sample and Data.

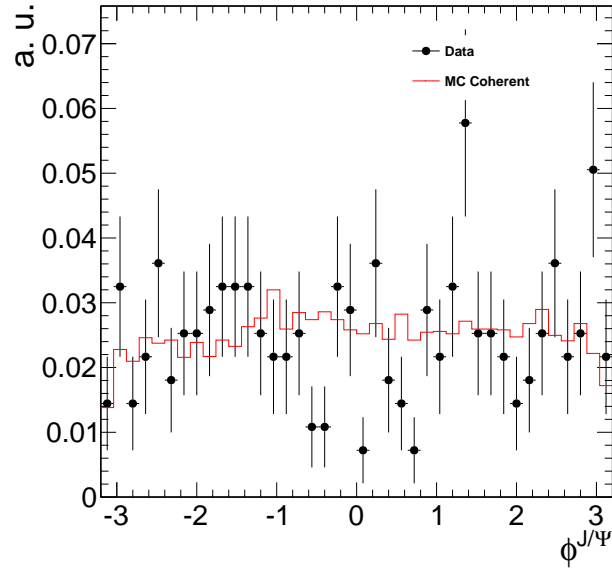


Figure 1.31: Comparison of the of the dimuon ϕ distributions between coherent MC sample and Data.

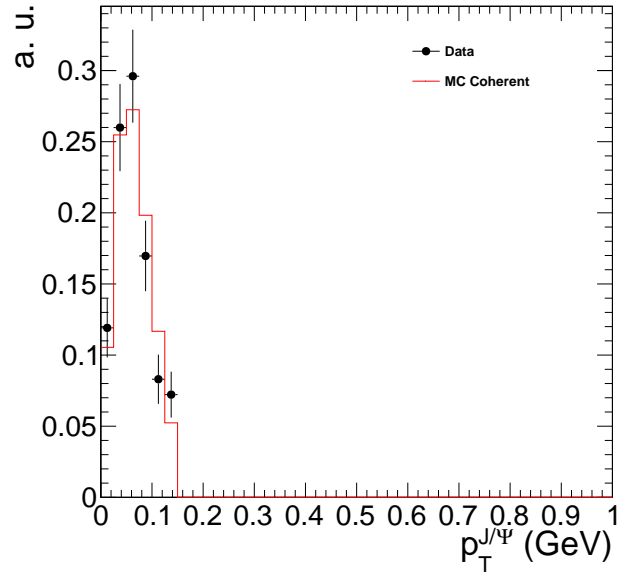


Figure 1.32: Comparison of the of the dimuon p_T distributions between coherent MC sample and Data.